Interface and transport properties of InN/VSi_2P_4 van der Waals magnetic heterostructures

Yijie Zhu [1,2] Meng Su,[1] Haoshen Ye [1] Dongmei Bai [3] and Jianli Wang [1,*]

[1]*School of Materials and Physics, China University of Mining and Technology, Xuzhou 221116, China*

[2]*National Laboratory of Solid State Microstructures and Department of Physics, Nanjing University, Nanjing 210093, China*

[3]*School of Mathematics, China University of Mining and Technology, Xuzhou 221116, China*

(Received 20 September 2022; revised 2 February 2023; accepted 29 August 2023; published 12 September 2023)

The interface itself becomes the device with increasing miniaturization in semiconductor spintronic devices. To obtain the interface and transport behaviors of novel low-dimensional spintronic devices, a fundamental physical understanding of the van der Waals magnetic system is highly desired. The interface and transport properties of the InN/VSi_2P_4 van der Waals magnetic heterostructure are studied systematically by combining first-principles calculations and Schrödinger-Poisson simulations. The VSi_2P_4 layer in the InN/VSi_2P_4 van der Waals heterostructure possesses unique electronic and magnetic properties such as a ferromagnetic ground state, stable easy magnetization axis, high Curie temperature, and high mobility. The semiconductor to half metal transition and significantly enhanced conductivities can be realized in the InN/VSi_2P_4 van der Waals heterostructure via electrostatic doping. The sheet carrier density can effectively modulate the conduction band distribution, the average charge position, and the interfacial electric fields of the InN/VSi_2P_4 van der Waals heterostructure. The capacitance of the InN/VSi_2P_4 van der Waals heterostructure increases with the sheet carrier density under a suitable voltage range. Our results indicate that the InN/VSi_2P_4 van der Waals heterostructure is a promising material for the low-dimensional spintronic devices.

DOI: 10.1103/PhysRevB.108.125413

I. INTRODUCTION

The graphenelike hexagonal indium nitride (g-InN) monolayer [1,2] possesses unique and fascinating properties such as superior thermal stability, large charge carrier mobility, strong light adsorption, and a tunable and sizable band gap. The smaller effective mass and narrower band gap bestow InN a higher electron mobility and higher saturation velocity than those of AlN and GaN [3,4]. However, the intrinsic nonmagnetism of the pristine g-InN monolayer restricts its application in future nanospintronic devices. The emergence of two-dimensional (2D) van der Waals (vdW) magnetic materials [5,6] offers new opportunities in the promising applications of g-InN-based spintronic devices. Ferromagnetism can be obtained for the g-InN monolayer through establishing a vdW heterostructure with 2D intrinsic ferromagnets, which could be applied for designing and developing novel low-dimensional spintronic devices. Although the optoelectronic properties of nitride-based nonmagnetic (NM) heterostructures have been investigated [7–9], the magnetic properties of nitride-based magnetic heterostructures have not received much attention yet. For nitride-based vdW magnetic heterostructures, the conductivities, the stability of the easy magnetization axis, and Curie temperature (T_c) can be modulated in the room-temperature spin valve based on VN/GaN/VN vdW heterostructures [10], the dual-gate field-effect transistors based on GaN/CrI_3 vdW heterostructures [11] and InN/VTe_2 vdW heterostructures [12].

The interface is a device in the post-Moore era, and the performance of the nanodevice is highly dependent on the interface properties. The interface polarization charge plays an extremely indispensable role in vdW heterostructures, which needs to be further studied in detail. We studied systematically the electronic and magnetic properties of the AlN/VSe_2 vdW heterostructure by combining first-principles calculations and Schrödinger-Poisson simulations [13]. Recently, a new class of 2D transition metal compounds represented by $MoSi_2N_4$ has been discovered [14–16], which possesses excellent physical properties. Some of them exhibit semiconductor properties with highly desirable intrinsic ferromagnetism, high Curie temperature, and magnetic anisotropy [16–20], which offers new opportunities in the promising applications of nitride-based spintronic devices. Here, we further explore the interface and transport properties of the InN/VSi_2P_4 vdW heterointerface based on our previous works. In Sec. III A, we discuss the electronic properties of the InN/VSi_2P_4 vdW heterostructure under biaxial strains and electrostatic doping. The magnetic anisotropy energy (MAE) and the T_c of the InN/VSi_2P_4 vdW heterostructure are simulated in Sec. III B. The transport property is a significant factor for the performance of low-dimensional spintronic devices, so in Sec. III C, we calculate the mobility and conductivity of the InN/VSi_2P_4 vdW heterostructure. By solving the one-dimensional Schrödinger-Poisson equations, we simulate the interface properties of the InN/VSi_2P_4 vdW heterostructure in Sec. III D.

II. METHODOLOGY

A. First-principles calculations

All of the structural optimization and electronic properties are performed by the first-principles density functional

*jlwang@cumt.edu.cn

theory (DFT) implemented in the Vienna *Ab-initio* Simulation Package [21]. The exchange-correlation interaction is treated based on the Perdew-Burke-Ernzerhof generalized gradient approximation (GGA) [22]. The DFT-D3 Grimme correction is also used for the consideration of long-range vdW interactions [23]. The vacuum space along the z axis is set to 30 Å in all computational processes to eliminate the interlayer interaction. The cutoff energy for the plane wave is set to 500 eV, and the convergence criteria for the total energy and maximum force are 10^{-5} eV and 0.01 eV/Å, respectively. A $12 \times 12 \times 1$ k-point mesh with the Monkhorst-Pack scheme is adopted for numerical integration over the Brillouin zone [24]. The phonon properties are carried out with $2 \times 2 \times 1$ supercells to check the stability of the structure [25]. The band structures are estimated by using the Heyd-Scuseria-Ernzerhof hybrid functional for more accurate values of the band gaps [26]. The GGA method is employed for the magnetic properties, and the influence of the Hubbard-U parameter [18,19,27–29] on the magnetic properties of the InN/VSi_2P_4 vdW heterostructure is checked in the Supplemental Material [30]. The effect of spin-orbital coupling (SOC) is considered when calculating the MAE [31,32], which is defined as the energy difference between out-of-plane and in-plane magnetization directions. The T_c of the InN/VSi_2P_4 vdW heterostructure is carried out by Monte Carlo simulations with $32 \times 32 \times 1$ supercells. The system is considered to reach equilibrium after 2×10^5 thermalizing steps, and the results are obtained after 4×10^5 loops. The electronic transport properties are performed using the semiclassical Boltzmann transport theory implemented in the BOLTZTRAP2 code [33].

B. One-dimensional Schrödinger-Poisson equations

The finite-difference forms of the one-dimensional Schrödinger equation and Poisson equation can be written as [34,35]

$$-\frac{\hbar^2}{2}\left[\frac{2(\psi_{i+1}-\psi_i)}{m^*_{i+1/2}h_i(h_i+h_{i-1})}-\frac{2(\psi_i-\psi_{i-1})}{m^*_{i-1/2}h_{i-1}(h_i+h_{i-1})}\right]=\lambda\psi_i \tag{1}$$

and

$$\frac{2\varepsilon_{i+1/2}(\phi_{i+1}-\phi_i)}{h_i(h_i+h_{i-1})}-\frac{2\varepsilon_{i-1/2}(\phi_i-\phi_{i-1})}{h_{i-1}(h_i+h_{i-1})}=-\frac{q(N_{Di}-n_i)}{\varepsilon_0}, \tag{2}$$

respectively. Here, m^*, ϕ, ψ, ε, ε_0, h_i, N_D, n, and λ stand for effective mass, electrostatic potential, wave function, static dielectric constant, vacuum dielectric constant, size of the ith mesh grid, ionized donor concentration, charge density, and eigenvalue, respectively. To obtain the electron distribution of the conduction band, the corresponding energy can be written as

$$V(z) = -q\phi_0(z) + \Delta E_c(z), \tag{3}$$

where ΔE_c is the conduction band offset at the heterointerface. The eigenvalue and wave function can be calculated by substituting the $V(z)$ corresponding to the test potential $\phi_0(z)$ into the Schrödinger equation. Then the charge density distribution $n(z)$ can be carried out by

$$n(z) = \frac{m^*}{\pi\hbar^2}\sum_{k=1}^{p}\psi_k^*(z)\psi_k(z)n_k\int_{E_k}^{\infty}\frac{1}{1+e^{\frac{E-E_F}{kT}}}dE, \tag{4}$$

where p and n_k are the numbers of the states and occupied electrons of the kth subband, respectively. By solving the Poisson equation, a new potential and conduction band energy can be obtained. Through repeated iterations, the self-consistent solution of the one-dimensional Schrödinger-Poisson equations can be found. The detailed solving process can be seen in the Supplemental Material [30].

III. RESULTS AND DISCUSSION

A. Electronic properties

The optimal lattice constants of monolayer InN and monolayer VSi_2P_4 are 3.58 and 3.46 Å, respectively. The monolayer InN is calculated to be an NM semiconductor with a direct band gap of 1.39 eV [12,30]. The monolayer VSi_2P_4 has a magnetic moment of $1.00\mu_B$ per unit cell, and the band gaps for the spin-up and spin-down channels are 0.56 and 1.19 eV, respectively [30]. All these results are in good agreement with other first-principles calculations for monolayer InN [1,2] and monolayer VSi_2P_4 [17,27]. The small lattice mismatch of 3.47% means it is possible to construct a high-quality vdW heterostructure. By comparing the binding energy of different stacking configurations, we find the most energetically favorable structure of the InN/VSi_2P_4 vdW heterostructure, as presented in Figs. 1(a) and 1(b). Detailed information can be seen in the Supplemental Material [30]. The optimal lattice constant of the InN/VSi_2P_4 vdW heterostructure is 3.51 Å, so the InN layer is compressed and the VSi_2P_4 layer is stretched. The InN/VSi_2P_4 vdW heterostructure inherits the ferromagnetic (FM) ground state from the monolayer VSi_2P_4 and has a magnetic moment of $0.94\mu_B$ per unit cell, mainly contributed by the vanadium atom. As can be seen in the charge density difference diagram, there is an obvious charge transfer at the InN/VSi_2P_4 vdW heterointerface. The VSi_2P_4 layer obtains $0.07e$ from the InN layer based on the Bader charge analysis [34,35], indicating the presence of interfacial interactions in the InN/VSi_2P_4 vdW heterostructure. As shown in Fig. 1(c), there are no obvious imaginary vibrational modes in the phonon spectra, indicating the stability of the InN/VSi_2P_4 vdW heterostructure. The band structure of the InN/VSi_2P_4 vdW heterostructure is illustrated in Fig. 1(d), and the orbital-projected band structure can be seen in the Supplemental Material [30]. The band gap of the spin-up channel is 1.02 eV, and for the spin-down channel, the band gap is 0.97 eV. For both spin channels, the conduction band minimum (CBM) and valence band maximum (VBM) are located at the M and Γ points, presenting indirect band gaps. The conduction band of the spin-up channel is mainly contributed by the V-e_g (d_{xy}, $d_{x^2-y^2}$) and V-e'_g (d_{xz}, d_{yz}) orbitals, and the valence band is dominated by the N-2p, P-3p, and V-a_{1g} (d_{z^2}) orbitals. The conduction band of the spin-down channel is contributed by the V-e_g and V-a_{1g} orbitals, and for the valence band, the main contribution comes from the N-2p and P-3p orbitals. The VSi_2P_4 monolayer has a direct band gap in the spin-up channel, but it turns into an indirect band gap after forming

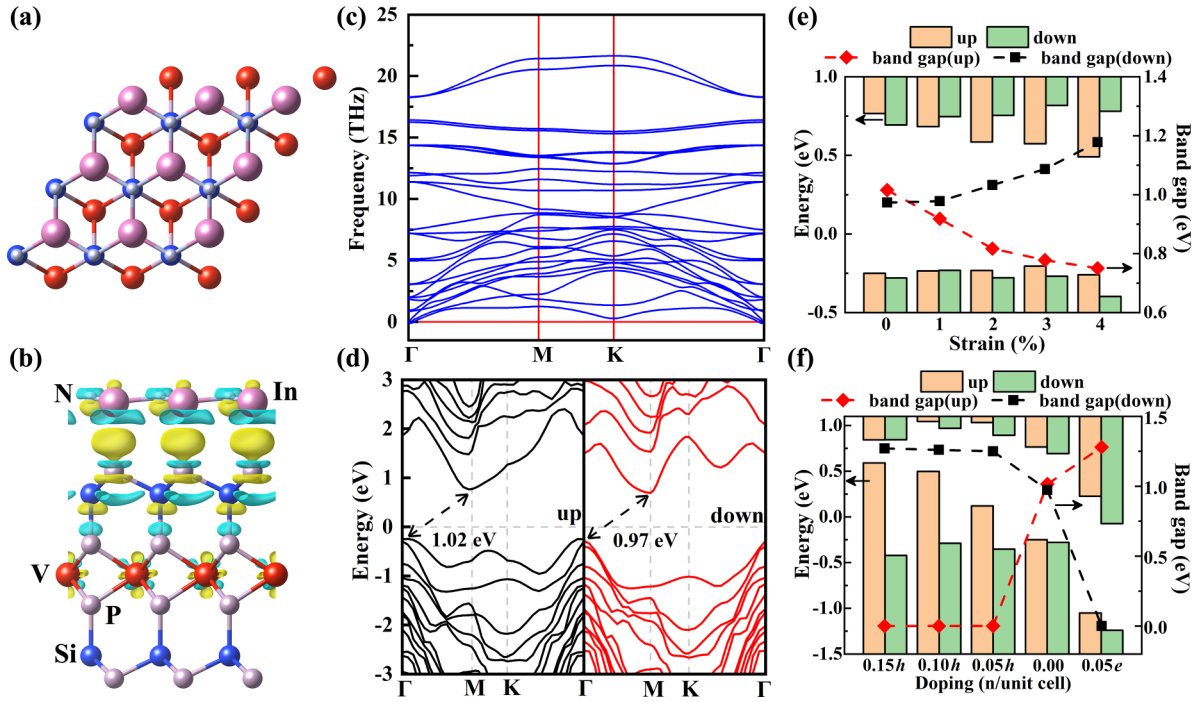

FIG. 1. (a), (b) The structure and charge density difference of the InN/VSi_2P_4 vdW heterostructure. The blue and yellow distributions represent the charge depletion and accumulation with an isosurface value of $0.005e$ Å^{-3}, respectively. (c) The phonon spectra of the InN/VSi_2P_4 vdW heterostructure. (d) The band structure of the InN/VSi_2P_4 vdW heterostructure. The CBM, VBM, and band gaps of the InN/VSi_2P_4 vdW heterostructure under different (e) strains and (f) doping concentrations.

a heterostructure with InN. The change of the band gap type is mainly contributed to the strain modulation caused by the lattice parameter and the interlayer interactions between the InN and VSi_2P_4 layers [30,36–41].

Applying in-plane biaxial strain is an effective method to modulate the electronic properties of 2D semiconductors [42,43]. The strain is defined as $\varepsilon = (a - a_0)/a_0 \times 100\%$, where a and a_0 represent the lattice constants after and before applying strain, respectively. The InN/VSi_2P_4 vdW heterostructure remains stable when ε ranges from 0% to 4%, and the corresponding phonon spectrum and band structures can be seen in the Supplemental Material [30]. The variations of CBM, VBM, and band gaps on the dependence of strain are illustrated in Fig. 1(e). When enhancing the stretch strain, the band gaps of the spin-up and spin-down channels decrease and increase, respectively. The band gap of the spin-up channel has a minimum value of 0.75 eV when $\varepsilon = 4\%$, and for the spin-down channel, the maximum value of the band gap is 1.18 eV. Biaxial strain changes the structure and charge distribution of the InN/VSi_2P_4 vdW heterostructure, and affects the orbital occupation and exchange integrals, eventually leading to the change in the band gap [30,44–47]. Note that when ε varies, the band gap remains indirect for both spin channels and the ferromagnetism is well preserved.

Besides strains, electrostatic doping has also been proven to be an effective way to modulate the carrier concentration and ferromagnetism of 2D semiconductors [48,49]. The variations of CBM, VBM, and band gaps on the dependence of doping concentration are illustrated in Fig. 1(f). We choose the maximum doping concentration of 1.40×10^{14} cm^{-2}, equivalent to 0.15 holes (h) or 0.15 electrons (e) per unit cell. In experiments, the doping concentration can be modulated up to 10^{13}–10^{15} cm^{-2} [50,51]. The InN/VSi_2P_4 vdW heterostructures are stable under $0.15h$/unit cell–$0.05e$/unit cell doping concentration [30]. When the number of electrons decreases (i.e., hole doping), the Fermi level decreases and the valence band crosses the Fermi level [30]. When the number of electrons increases (i.e., electron doping), the Fermi level increases and the conduction band crosses the Fermi level [30]. Therefore, the InN/VSi_2P_4 vdW heterostructure can realize a semiconductor to half metal transition by electrostatic doping.

B. Magnetic properties

The MAE plays an invaluable role in the magnetic properties of ferromagnets, which is calculated by comparing the energy along different magnetization directions [31,32]. The MAE of the InN/VSi_2P_4 vdW heterostructure under different strains and doping concentrations is depicted in Figs. 2(a) and 2(b). The polar angle θ represents the angle between the magnetization direction and xy plane; $\theta = 0^\circ$ and 90° represent the spin along the x axis and z axis, respectively. The InN/VSi_2P_4 vdW heterostructure has an MAE of 0.12 meV. When enhancing the stretch strain, the MAE decreases and has a minimum value of 0.06 meV at $\varepsilon = 4\%$. The MAE is reduced under both hole and electron doping, and reaches the minimum value of 0.07 meV under $0.15h$ doping. Based on the second-order perturbation theory [34], the MAE can be written as

$$\Delta E = \pm\xi^2 \sum_{o,u} \frac{|\langle o|L_z|u\rangle|^2}{E_u - E_o}, \tag{5}$$

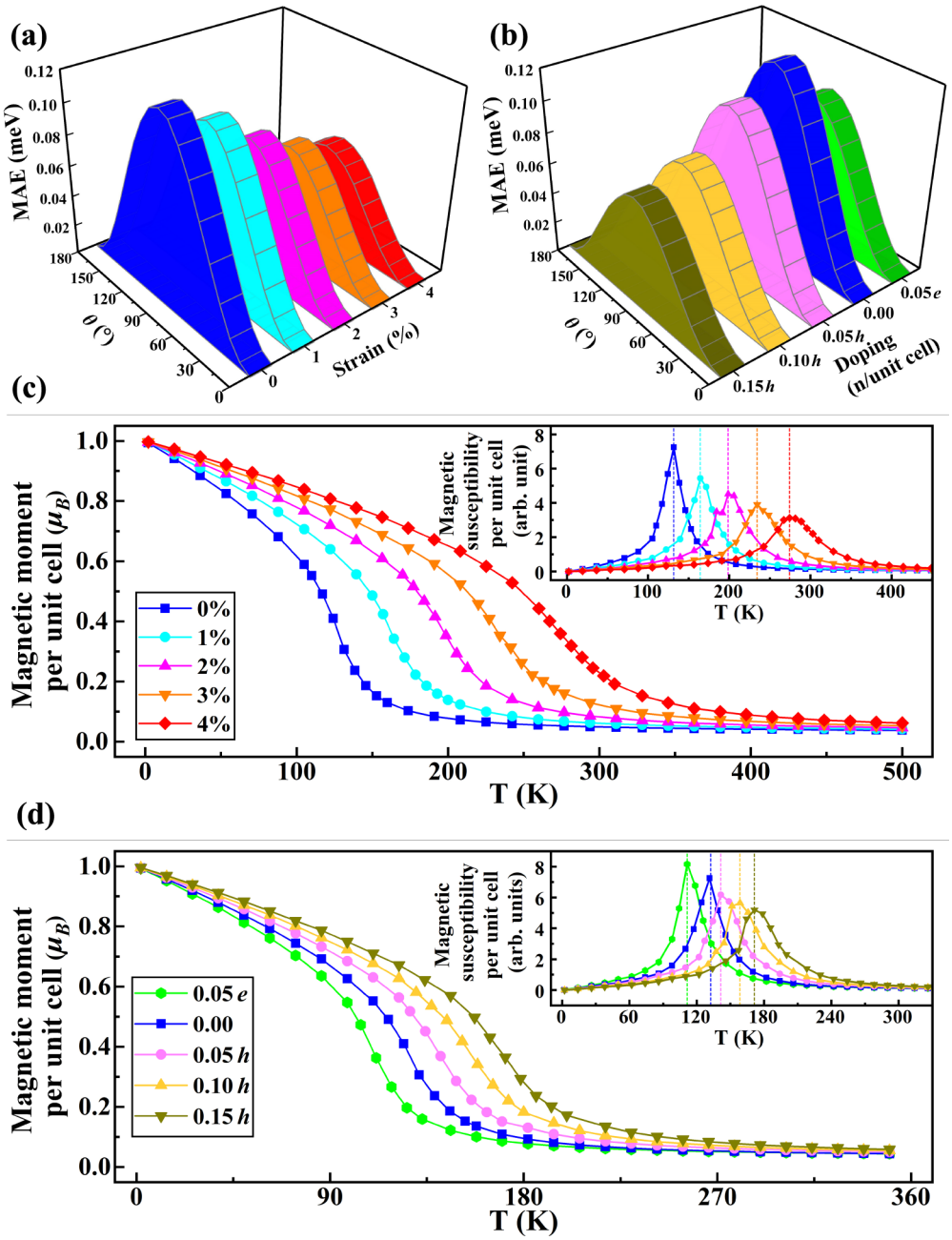

FIG. 2. The MAE of the InN/VSi_2P_4 vdW heterostructure under variable (a) strains and (b) doping concentrations. The polar angle θ is the angle between the magnetization direction and the xy plane. The Monte Carlo simulations of the magnetic moment and magnetic susceptibility per unit cell of the InN/VSi_2P_4 vdW heterostructure for different (c) strains and (d) doping concentrations.

where ξ is the SOC constant; + (–) denotes the same (opposite) spin directions of the occupied (o) and unoccupied (u) states; E_u and E_o represent the corresponding energy levels. As depicted in Fig. S11 [30], the MAE is mainly contributed by the SOC interaction of V-d_{xy} and V-$d_{x^2-y^2}$ orbitals, changing negligibly under the strain and electrostatic doping. There are only five nonzero angular momentum matrix elements between the d states: $\langle d_{z^2}|L_x|d_{yz}\rangle$, $\langle d_{xy}|L_x|d_{xz}\rangle$, $\langle d_{x^2-y^2}|L_x|d_{yz}\rangle$, $\langle d_{xz}|L_z|d_{yz}\rangle$, and $\langle d_{x^2-y^2}|L_z|d_{xy}\rangle$. Only states near the Fermi level need to be considered when discussing the contribution of orbital exchange interactions to the MAE since MAE is inversely proportional to the energy difference between the occupied and unoccupied states. As can be seen in Fig. 1(d), the bands near the Fermi level are mainly dominated by the V-e_g and V-a_{1g} orbitals. Although there is a SOC interaction between the e_g' and a_{1g} orbitals, its contribution to the MAE is negligible because the e_g' states are far away from the Fermi level. Therefore, the SOC interactions of e_g states play a decisive role in MAE. It is worth noting that the MAE is always positive under all modulating conditions, so the easy magnetization axis maintains in the xy plane. The MAE value of 0.12 meV is also larger than those of other 2D materials, such as Cr_2S_3 (0.08 meV) [52], $MnBi_2Te_4$ (0.10 meV) [53], Mn_2NF_2 (0.002 meV) [54], Mn_2NO_2 (0.06 meV) [54], $CrCl_3$ (0.025 meV) [55], and so on.

The T_c is an important parameter for measuring the performance of ferromagnets since the system will turn into a paramagnetic state and lose the original properties when the ambient temperature is higher than T_c. Based on the Heisenberg model, we perform a Monte Carlo simulation to calculate the T_c of the InN/VSi_2P_4 vdW heterostructure [10,56]. The spin Hamiltonian is defined as follows,

$$H = -J\sum_{i,j} S_i \cdot S_j - A\sum_i \left(S_i^z\right)^2, \tag{6}$$

where J is the nearest magnetic exchange parameter, S_i and S_j are the spins of sites i and j, A is the MAE mentioned above, and S_i^z is the spin component of site i along the easy magnetization axis. The energy of the InN/VSi_2P_4 vdW heterostructure with FM and antiferromagnetic (AFM) configurations can be written as

$$E_{\mathrm{FM}} = E_0 - 3J|S|^2 - A|S|^2 \tag{7}$$

and

$$E_{\mathrm{AFM}} = E_0 + J|S|^2 - A|S|^2. \tag{8}$$

So the nearest magnetic exchange parameter J can be obtained by

$$J = -\frac{E_{\mathrm{FM}} - E_{\mathrm{AFM}}}{4|S|^2}, \tag{9}$$

where S and E_0 indicate the magnetic moment per unit cell and the energy without magnetic coupling, respectively. The dependences of the magnetic moment and magnetic susceptibility on temperature are depicted in Figs. 2(c) and 2(d) for varied strains and doping concentrations, respectively. The T_c of the InN/VSi_2P_4 vdW heterostructure is calculated to be 131 K, which can be modulated up to 274 K under 4% strain and 171 K under a $0.15h$ doping concentration because both stretch strain and hole doping enhance the superexchange interaction and increase the exchange parameter J [11,57]. The T_c of 274 K is much larger than other FM heterostructures, such as $Cr_2Ge_2Te_6/NiO$ (120 K) [58], $Cr_2Ge_2Te_6/Sc_2CO_2$ (92 K) [59], $CrI_3/MoTe_2$ (60 K) [60], and CrI_3/SiC (62 K) [61]. To conclude, the InN/VSi_2P_4 vdW heterostructure possesses both a high T_c near room temperature under strain and a stable easy magnetization axis, which makes it a good candidate for spintronics devices.

C. Transport properties

The InN/VSi_2P_4 vdW heterostructure can be modulated into a half metal under electrostatic doping, so the electron transport properties of the system will change considerably, which is also crucial for the practical applications of spintronic devices. The conductivity along the α direction can be calculated by [33]

$$\sigma_{\alpha\alpha} = \frac{e^2}{V}\int \tau v_\alpha^2 \left[-\frac{\partial f_0(T,E)}{\partial E}\right] dE, \tag{10}$$

where V, v_α, $f_0(T,E)$, and T represent the volume of unit cells, group velocity, the Fermi-Dirac distribution function, and temperature, respectively. Based on the deformation potential theory [62], the reference relaxation time can be depicted as

$$\tau = \frac{\hbar^3 C_{2\mathrm{D}}}{k_B T m_d (E_l)^2}, \tag{11}$$

where $C_{2\mathrm{D}}$, m_d, and E_l are the 2D elastic modulus, average effective mass, and deformation potential constant, respectively. The elastic modulus of the 2D materials is defined as

$$C_{2\mathrm{D}} = \frac{1}{S_0}\frac{d^2\Delta E}{dl^2}, \tag{12}$$

where ΔE and S_0 stand for the energy difference after applying a small strain l and the lattice volume of the 2D system at equilibrium, respectively. The average effective mass is defined as

$$m_d = \sqrt{m_x^* m_y^*}, \tag{13}$$

where the x and y directions correspond to the zigzag and armchair directions, respectively. The effective mass along the specific direction α can be calculated by

$$\frac{1}{m^*} = \frac{1}{\hbar^2}\frac{\partial^2 E}{\partial k_\alpha^2}, \tag{14}$$

where k_α is the wave vector. The deformation potential constant of the electrons at the CBM and VBM can be expressed as

$$E_l^{\mathrm{CBM(VBM)}} = \Delta V_{\mathrm{CBM(VBM)}}\frac{a_0}{\Delta a}, \tag{15}$$

where $\Delta V_{\mathrm{CBM(VBM)}}$ is the energy difference between the CBM and VBM under an applied strain, a_0 is the lattice constant, and Δa is the change of a_0 caused by strain. The calculated parameters are illustrated in Table I. Furthermore, the mobility of the carriers μ can be obtained via $\mu = \tau e/m^*$, where τ and m^* are the relaxation time and effective mass of carriers, respectively. The dependence of mobility on temperature is presented in Fig. 3. The mobilities of the spin-up carriers of monolayer VSi_2P_4 are lower than the spin-down carriers, which is mainly attributed to the large deformation potential constant. Compared with monolayer InN and monolayer VSi_2P_4, the mobilities of the InN/VSi_2P_4 vdW heterostructure are significantly enhanced. Due to the low effective mass of holes, the spin-up channel of the InN/VSi_2P_4 vdW heterostructure has a high hole mobility of 2402 $\mathrm{cm^2\,V^{-1}\,s^{-1}}$ along the zigzag direction, which is much higher than other 2D materials, such as MoS_2 (200 $\mathrm{cm^2\,V^{-1}\,s^{-1}}$) [63], $MoSi_2As_4$ (1100 $\mathrm{cm^2\,V^{-1}\,s^{-1}}$) [64], VSe_2 (307 $\mathrm{cm^2\,V^{-1}\,s^{-1}}$) [65], Zr_2CO_2 (2300 $\mathrm{cm^2\,V^{-1}\,s^{-1}}$) [66], Hf_2CO_2 (2271 $\mathrm{cm^2\,V^{-1}\,s^{-1}}$) [66], and so on.

Figure 4 presents the conductivities of the InN/VSi_2P_4 vdW heterostructure along the zigzag and armchair directions for both spin channels. As the temperature increases, the conductivity tends to decrease due to the influence of thermal excitation. The valence band for the spin-up channel of the InN/VSi_2P_4 vdW heterostructure crosses the Fermi level under 0.05–$0.15h$/unit cell doping, leading to higher conductivities of the spin-up carriers than the spin-down carriers. The absence of spin-down states under hole doping means a pure spin-up polarized current can be realized in the InN/VSi_2P_4 vdW heterostructure. As for electron doping, the conduction band of the spin-down channel crosses the Fermi level while

TABLE I. Calculated parameters of monolayer InN, monolayer VSi_2P_4, and the InN/VSi_2P_4 vdW heterostructure: The elastic modulus C_{2D}, the effective mass m^*, and the deformation potential constant E_l. The results of different spin channels are separated by the slashes.

Material	C_{2D} (N/m)	Direction	m_e^* (m_e)	m_h^* (m_e)	E_l^e (eV)	E_l^h (eV)
InN	96.75	Zigzag	0.15/0.15	0.63/0.63	−9.14/ − 9.14	−4.82/ − 4.82
		Armchair	0.47/0.47	1.00/1.00	−8.08/ − 8.08	−2.52/ − 2.52
VSi_2P_4	194.62	Zigzag	1.39/2.11	2.10/0.65	−7.32/2.31	−2.16/ − 2.57
		Armchair	6.71/0.78	2.23/0.59	−7.33/ − 3.32	−6.78/ − 7.65
InN/VSi_2P_4	279.64	Zigzag	1.14/1.71	0.65/0.70	−6.70/ − 2.77	−2.11/ − 1.92
		Armchair	1.92/0.63	3.88/5.48	−3.11/2.99	−3.82/ − 0.92

the spin-up channel is almost insulated due to the large band gap. For the spin-up channel, the conductivities along the zigzag direction are about ten times higher than that along the armchair direction owing to the low effective mass, while for the spin-down channel, the conductivities along the zigzag and armchair directions are almost the same.

D. Interface properties

Based on the parameters obtained by the first-principles calculations, numerically solving the Schrödinger-Poisson equation is an effective method to predict the carrier distribution in vdW heterostructures [34,35]. The heterostructure model, boundary condition, and specific parameters are adjustable and flexible throughout the Schrödinger-Poisson simulation [67]. According to the above results and the Bader charge analysis, there is significant charge transfer and charge interaction at the InN/VSi_2P_4 vdW heterointerface. A 10 Å-InN/10 Å-VSi_2P_4/10 Å-InN vdW heterostructure is constructed based on the stacking tests, and detailed information can be seen in the Supplemental Material [30]. The 2D electron gas in the semiconductor heterostructure is mainly caused by the conduction band offset and the discontinuous spontaneous polarization (P_S) and piezoelectric polarization (P_P) at the interface [68,69]. The total polarization difference at the interface can be written as [13,70]

$$\Delta P = P_P(\mathrm{InN}) + P_S(\mathrm{InN}) - P_S(\mathrm{VSi_2P_4}). \tag{16}$$

The conduction band offset is calculated based on the heterostructure constructed by the InN bilayer and VSi_2P_4 monolayer. The doping concentration of 1×10^{12} cm^{-3} and a positive polarization are set for one side of the InN layer.

The distributions of the conduction band and wave function along the z direction for the different spin channels of the InN/VSi_2P_4 vdW heterostructure are illustrated in Figs. 5(a) and 5(b), and N_s varies from 5×10^{12} to 25×10^{12} cm^{-2}, which is comparable to the experimental values [71,72]. The insets show the atomic structure of the InN/VSi_2P_4/InN vdW heterojunction. The polarization and sheet carrier density at the interface break the original symmetry so that the conduction band and wave function are both asymmetrical. The charge density distribution shares the same trend with the wave function since there is only one bound state in this system. For both spin channels, the conduction band tends to tilt and the wave function tends to disperse when N_s increases. The wave function of the spin-down channel varies more

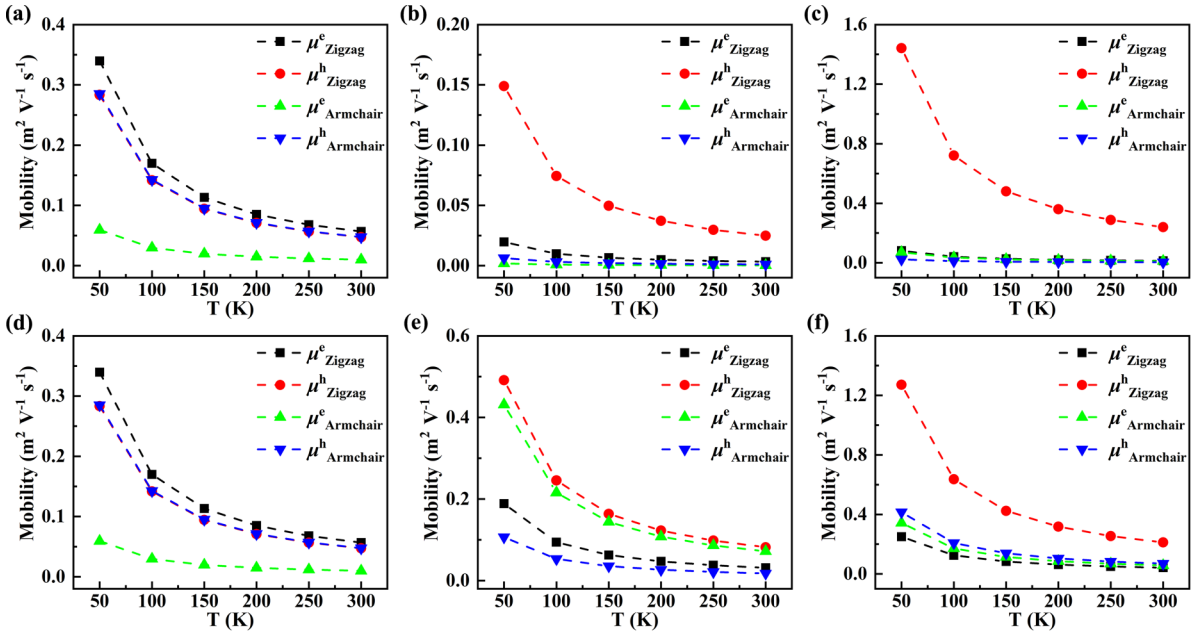

FIG. 3. The mobilities for the spin-up channel of the (a) monolayer InN, (b) monolayer VSi_2P_4, and (c) InN/VSi_2P_4 vdW heterostructure. The mobilities for the spin-down channel of the (d) monolayer InN, (e) monolayer VSi_2P_4, and (f) InN/VSi_2P_4 vdW heterostructure.

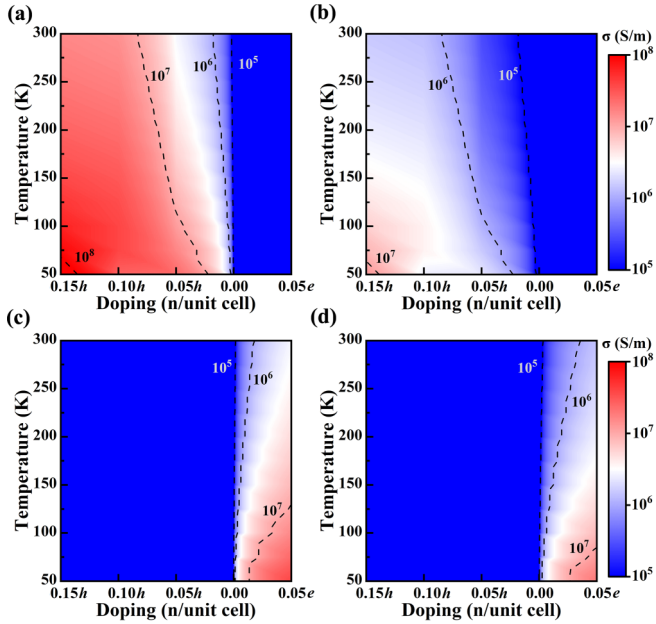

FIG. 4. The conductivities along the zigzag direction for the (a) spin-up and (b) spin-down channels of the InN/VSi_2P_4 vdW heterostructure under variable temperatures and doping concentrations. (c), (d) The corresponding conductivities along the armchair direction.

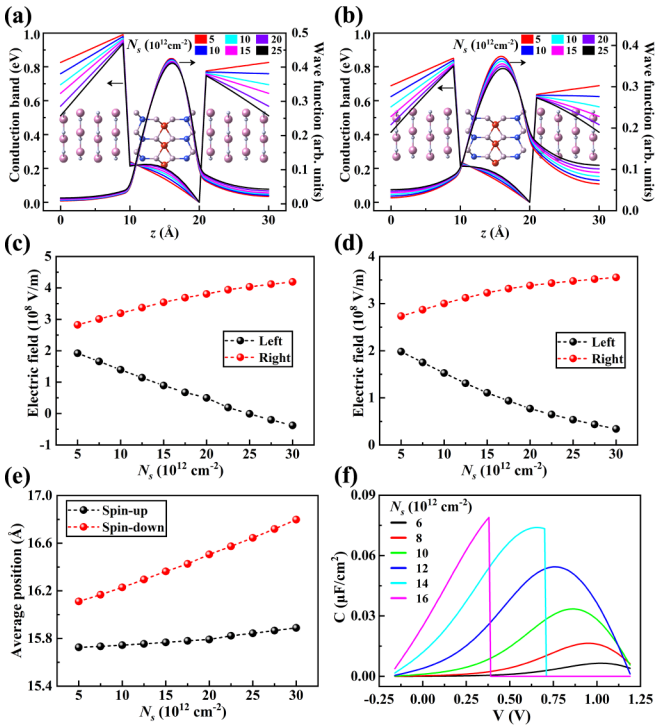

FIG. 5. The simulated conduction band and wave function for the (a) spin-up and (b) spin-down channels of the InN/VSi_2P_4 vdW heterostructure with varied N_s: $m^*(\mathrm{InN}) = 0.23m_e$, $m^*(\mathrm{VSi_2P_4\text{-up}}) = 3.05m_e$, $m^*(\mathrm{VSi_2P_4\text{-down}}) = 1.28m_e$, $\varepsilon_s(\mathrm{InN}) = 6.97$, $\varepsilon_s(\mathrm{VSi_2P_4}) = 7.82$, $\Delta E_c(\mathrm{up}) = 0.77$ eV, and $\Delta E_c(\mathrm{down}) = 0.63$ eV. The interface electric fields for the (c) spin-up and (d) spin-down channels under different N_s. (e) The average position of electrons when N_s varies. (f) The simulated C-V characteristics of the InN/VSi_2P_4 vdW heterostructure with varied N_s.

for different N_s, which is mainly attributed to the shallower potential well and lower effective mass compared with the spin-up channel. Due to the conduction band offset and the discontinuous potential, there are two equivalent electric fields at the heterointerfaces. The dependence of interface electric fields on N_s is shown in Figs. 5(c) and 5(d). For both spin channels, the electric fields at the left and right interfaces decrease and increase linearly with N_s, respectively. As N_s varies, the electric field for the spin-up channel varies over a larger range because of the larger conduction band offset, and the direction of the electric field at the left interface inverses when N_s is about 25×10^{12} cm^{-2}.

To describe the confinement of the potential well to electrons, Fig. 5(e) shows the relationship between N_s and the average position of electrons, which is defined as

$$\bar{z} = \int_0^L z\psi^*(z)\psi(z)dz, \tag{17}$$

where L is the thickness of the InN/VSi_2P_4 vdW heterostructure. When N_s increases, the potential of the barrier tends to decrease and some electrons will occupy high-energy levels, so it will be harder for the heterostructure to confine the electrons. For different N_s, the average position of the electrons moves by a distance of approximately 0.1 and 0.7 Å for the spin-up and spin-down channels, respectively. Compared with the spin-up channel, it is more difficult to restrict the spin-down electron owing to the shallower potential well and smaller effective mass.

The capacitance-voltage (C-V) characteristic is an important measure of the electric properties and interface quality of vdW heterostructures [73,74]. The C-V characteristic is calculated by setting the boundary conditions that $\phi(0) = V_0$ and $\phi(L) = 0$, where V_0 is the sum of the built-in and applied reverse-bias voltages. When two different voltages are successively applied and they differ by a small increment ΔV, the increment of the charge can be written as [75,76]

$$\Delta Q = -\int_0^L q[n_2(z) - n_1(z)]dz, \tag{18}$$

where 1 and 2 represent the results for the first and second applied voltages. Then the capacitance is given by

$$C = \frac{\Delta Q}{\Delta V}. \tag{19}$$

The C-V characteristic of the InN/VSi_2P_4 vdW heterostructure is illustrated in Fig. 5(f). As the voltage increases, the value of the capacitance first increases and then decreases. When N_s increases, the value of the capacitance also increases under the same voltage. It is worth noting that when N_s is larger than 14×10^{12} cm^{-2}, the capacitance will suddenly change to zero at a certain voltage value. Due to the shallow potential well and small band offset of the InN/VSi_2P_4 vdW heterostructure, as N_s increases, it is more difficult to confine the electrons and more susceptible to breakdown.

IV. CONCLUSION

The transport and interface properties of the InN/VSi_2P_4 vdW magnetic semiconductor heterostructure are systematically investigated by combining the density functional theory

calculations and Schrödinger-Poisson simulations, which are imperative in the design of new nanospintronic devices. The magnetic ground state of the InN/VSi_2P_4 vdW heterostructure is FM and the easy magnetization axis is in the xy plane, both remaining unchanged under biaxial strains and electrostatic doping. The InN/VSi_2P_4 vdW heterostructure can be transformed into a half metal by hole doping and electron doping. The T_c of the InN/VSi_2P_4 vdW heterostructure is calculated to be 131 K by Monte Carlo simulation, which can be increased up to 274 and 171 K under 4% strain and $0.15h$ doping concentration, respectively. Compared with monolayer InN and monolayer VSi_2P_4, the mobilities of the InN/VSi_2P_4 vdW heterostructure are significantly enhanced. Meanwhile, electrostatic doping leads to a significant increase in the conductivity of the InN/VSi_2P_4 vdW heterostructure. The interface property is further investigated through the Schrödinger-Poisson simulation since there is an obvious charge transfer and orbital hybridization at the InN/VSi_2P_4 vdW heterointerface. Compared with the spin-up channel, it is more difficult to restrict the spin-down electrons when N_s varies owing to the shallower potential well and lower effective mass. When N_s increases, the capacitance of the InN/VSi_2P_4 vdW heterostructure increases at the same voltage, but it will be more susceptible to breakdown at the same time. Our result indicates that the InN/VSi_2P_4 vdW heterostructure is a promising material for low-dimensional spintronic devices owing to its FM ground state, high T_c, stable easy magnetization axis, high mobility, and strong conductivity.

ACKNOWLEDGMENTS

This work has been supported by Key Academic Discipline Project of China University of Mining and Technology under Grant No. 2022WLXK02.

[1] H. Şahin, S. Cahangirov, M. Topsakal, E. Bekaroglu, E. Akturk, R. T. Senger, and S. Ciraci, Monolayer honeycomb structures of group-IV elements and III-V binary compounds: First-principles calculations, Phys. Rev. B **80**, 075305 (2009).

[2] H. L. Zhuang, A. K. Singh, and R. G. Hennig, Computational discovery of single-layer III-V materials, Phys. Rev. B **87**, 165415 (2013).

[3] M. S. Prete, O. Pulci, and F. Bechstedt, Strong in- and out-of-plane excitons in two-dimensional InN nanosheets, Phys. Rev. B **98**, 235431 (2018).

[4] J. Wu, When group-III nitrides go infrared: New properties and perspectives, J. Appl. Phys. **106**, 011101 (2009).

[5] C. Gong, L. Li, Z. Li, H. Ji, A. Stern, Y. Xia, T. Cao, W. Bao, C. Wang, Y. Wang, Z. Q. Qiu, R. J. Cava, S. G. Louie, J. Xia, and X. Zhang, Discovery of intrinsic ferromagnetism in two-dimensional van der Waals crystals, Nature (London) **546**, 265 (2017).

[6] B. Huang, G. Clark, E. Navarro-Moratalla, D. R. Klein, R. Cheng, K. L. Seyler, D. Zhong, E. Schmidgall, M. A. McGuire, D. H. Cobden, W. Yao, D. Xiao, P. Jarillo-Herrero, and X. Xu, Layer-dependent ferromagnetism in a van der Waals crystal down to the monolayer limit, Nature (London) **546**, 270 (2017).

[7] J. Wang, H. Shu, P. Liang, N. Wang, D. Cao, and X. Chen, Thickness-dependent phase stability and electronic properties of GaN nanosheets and MoS_2/GaN van der Waals heterostructures, J. Phys. Chem. C **123**, 3861 (2019).

[8] H. Henck, Z. Ben Aziza, O. Zill, D. Pierucci, C. H. Naylor, M. G. Silly, N. Gogneau, F. Oehler, S. Collin, J. Brault, F. Sirotti, F. Bertran, P. Le Fèvre, S. Berciaud, A. T. C. Johnson, E. Lhuillier, J. E. Rault, and A. Ouerghi, Interface dipole and band bending in the hybrid $p-n$ heterojunction MoS_2/GaN(0001), Phys. Rev. B **96**, 115312 (2017).

[9] M. A. Hassan, M.-W. Kim, M. A. Johar, A. Waseem, M.-K. Kwon, and S.-W. Ryu, Transferred monolayer MoS_2 onto GaN for heterostructure photoanode: Toward stable and efficient photoelectrochemical water splitting, Sci. Rep. **9**, 20141 (2019).

[10] H. Ye, Y. Zhu, D. Bai, J. Zhang, X. Wu, and J. Wang, Spin valve effect in VN/GaN/VN van der Waals heterostructures, Phys. Rev. B **103**, 035423 (2021).

[11] H. Ye, X. Wang, D. Bai, J. Zhang, X. Wu, G. P. Zhang, and J. Wang, Significant enhancement of magnetic anisotropy and conductivity in GaN/CrI_3 van der Waals heterostructures via electrostatic doping, Phys. Rev. B **104**, 075433 (2021).

[12] J. Sun, F. Pei, D. Bai, J. Zhang, and J. Wang, Room temperature ferromagnetism and transport properties in InN/VTe_2 van der Waals heterostructures, Appl. Surf. Sci. **598**, 153781 (2022).

[13] Y. Zhu, D. Zhang, H. Ye, D. Bai, M. Li, G. P. Zhang, J. Zhang, and J. Wang, Magnetic and Electronic Properties of AlN/VSe_2 van der Waals Heterostructures from Combined First-Principles and Schrödinger-Poisson Simulations, Phys. Rev. Appl. **18**, 024012 (2022).

[14] Y.-L. Hong, Z. Liu, L. Wang, T. Zhou, W. Ma, C. Xu, S. Feng, L. Chen, M.-L. Chen, D.-M. Sun, X.-Q. Chen, H.-M. Cheng, and W. Ren, Chemical vapor deposition of layered two-dimensional $MoSi_2N_4$ materials, Science **369**, 670 (2020).

[15] L. Wang, Y. Shi, M. Liu, A. Zhang, Y.-L. Hong, R. Li, Q. Gao, M. Chen, W. Ren, H.-M. Cheng, Y. Li, and X.-Q. Chen, Intercalated architecture of MA_2Z_4 family layered van der Waals materials with emerging topological, magnetic and superconducting properties, Nat. Commun. **12**, 2361 (2021).

[16] J. Chen and Q. Tang, The versatile electronic, magnetic and photo-electro catalytic activity of a new 2D MA_2Z_4 family, Chem. Eur. J. **27**, 9925 (2021).

[17] Y. Feng, Z. Wang, X. Zuo, and G. Gao, Electronic phase transition, spin filtering effect, and spin Seebeck effect in 2D high-spin-polarized VSi_2X_4 (X = N, P, As), Appl. Phys. Lett. **120**, 092405 (2022).

[18] M. R. K. Akanda and R. K. Lake, Magnetic properties of $NbSi_2N_4$, VSi_2N_4, and VSi_2P_4 monolayers, Appl. Phys. Lett. **119**, 052402 (2021).

[19] S. Li, Q. Wang, C. Zhang, P. Guo, and S. A. Yang, Correlation-driven topological and valley states in monolayer VSi_2P_4, Phys. Rev. B **104**, 085149 (2021).

[20] H. Ye, L. Liu, D. Bai, G. P. Zhang, J. Zhang, and J. Wang, Room-temperature spin valve effect in $TiCr_2N_4$ monolayer, J. Mater. Chem. C **10**, 12422 (2022).

[21] G. Kresse and J. Furthmüller, Efficient iterative schemes for *ab initio* total-energy calculations using a plane-wave basis set, Phys. Rev. B **54**, 11169 (1996).

[22] J. P. Perdew, K. Burke, and M. Ernzerhof, Generalized Gradient Approximation Made Simple, Phys. Rev. Lett. **77**, 3865 (1996).

[23] S. Grimme, J. Antony, S. Ehrlich, and H. Krieg, A consistent and accurate ab initio parametrization of density functional dispersion correction (DFT-D) for the 94 elements H-Pu, J. Chem. Phys. **132**, 154104 (2010).

[24] H. J. Monkhorst and J. D. Pack, Special points for Brillouin-zone integrations, Phys. Rev. B **13**, 5188 (1976).

[25] A. Togo and I. Tanaka, First principles phonon calculations in materials science, Scr. Mater. **108**, 1 (2015).

[26] J. Heyd, G. E. Scuseria, and M. Ernzerhof, Hybrid functionals based on a screened Coulomb potential, J. Chem. Phys. **118**, 8207 (2003).

[27] X. Feng, X. Xu, Z. He, R. Peng, Y. Dai, B. Huang, and Y. Ma, Valley-related multiple Hall effect in monolayer VSi_2P_4, Phys. Rev. B **104**, 075421 (2021).

[28] F. Aryasetiawan, K. Karlsson, O. Jepsen, and U. Schönberger, Calculations of Hubbard U from first-principles, Phys. Rev. B **74**, 125106 (2006).

[29] L. Vaugier, H. Jiang, and S. Biermann, Hubbard U and Hund exchange J in transition metal oxides: Screening versus localization trends from constrained random phase approximation, Phys. Rev. B **86**, 165105 (2012).

[30] See Supplemental Material at https://link.aps.org/supplemental/10.1103/PhysRevB.108.125413 for (I) structural configuration and magnetic ground states tests, (II) electronic and magnetic properties of the InN/VSi_2P_4 vdW heterostructure, (III) GGA + U test of the monolayer VSi_2P_4 and InN/VSi_2P_4 vdW heterostructure, and (IV) details for the interface properties of the InN/VSi_2P_4 vdW heterostructure, which includes Refs. [40,41].

[31] G. H. Daalderop, P. J. Kelly, and M. F. Schuurmans, First-principles calculation of the magnetocrystalline anisotropy energy of iron, cobalt, and nickel, Phys. Rev. B **41**, 11919 (1990).

[32] D. Wang, R. Wu, and A. J. Freeman, First-principles theory of surface magnetocrystalline anisotropy and the diatomic-pair model, Phys. Rev. B **47**, 14932 (1993).

[33] G. K. H. Madsen, J. Carrete, and M. J. Verstraete, BoltzTraP2, a program for interpolating band structures and calculating semi-classical transport coefficients, Comput. Phys. Commun. **231**, 140 (2018).

[34] I. H. Tan, G. L. Snider, L. D. Chang, and E. L. Hu, A self-consistent solution of Schrödinger–Poisson equations using a nonuniform mesh, J. Appl. Phys. **68**, 4071 (1990).

[35] Q. Fanyao, A. L. A. Fonseca, and O. A. C. Nunes, Stokes shift in one-side modulation-n-doped-strained $Ga_xIn_{1-x}As/InP$ asymmetric quantum well, Superlattices Microstruct. **26**, 377 (1999).

[36] Z. Huang, X. Qi, H. Yang, C. He, X. Wei, X. Peng, and J. Zhong, Band-gap engineering of the h-BN/MoS_2/h-BN sandwich heterostructure under an external electric field, J. Phys. D: Appl. Phys. **48**, 205302 (2015).

[37] X. Hu, L. Kou, and L. Sun, Stacking orders induced direct band gap in bilayer $MoSe_2$-WSe_2 lateral heterostructures, Sci. Rep. **6**, 31122 (2016).

[38] K. Lai, H. Li, Y.-K. Xu, W.-B. Zhang, and J. Dai, Achieving a direct band gap and high power conversion efficiency in an SbI_3/BiI_3 type-II vdW heterostructure via interlayer compression and electric field application, Phys. Chem. Chem. Phys. **21**, 2619 (2019).

[39] Y. Bai, Q. Zhang, N. Xu, K. Deng, and E. Kan, Efficient carrier separation and band structure tuning of two-dimensional C_2N/GaTe van der Waals heterostructure, J. Phys. Chem. C **122**, 15892 (2018).

[40] R. F. W. Bader, A quantum theory of molecular structure and its applications, Chem. Rev. **91**, 893 (1991).

[41] E. Sanville, S. D. Kenny, R. Smith, and G. Henkelman, Improved grid-based algorithm for Bader charge allocation, J. Comput. Chem. **28**, 899 (2007).

[42] H. Shi, H. Pan, Y. W. Zhang, and B. I. Yakobson, Quasiparticle band structures and optical properties of strained monolayer MoS_2 and WS_2, Phys. Rev. B **87**, 155304 (2013).

[43] M. M. Obeid, Tuning the electronic and optical properties of Type-I PbI_2/α-tellurene van der Waals heterostructure via biaxial strain and external electric field, Appl. Surf. Sci. **508**, 144824 (2020).

[44] X. Peng, Q. Wei, and A. Copple, Strain-engineered direct-indirect band gap transition and its mechanism in two-dimensional phosphorene, Phys. Rev. B **90**, 085402 (2014).

[45] X. Peng and A. Copple, Origination of the direct-indirect band gap transition in strained wurtzite and zinc-blende GaAs nanowires: A first principles study, Phys. Rev. B **87**, 115308 (2013).

[46] R. Nelson, C. Ertural, J. George, V. L. Deringer, G. Hautier, and R. Dronskowski, LOBSTER: Local orbital projections, atomic charges, and chemical-bonding analysis from projector-augmented-wave-based density-functional theory, J. Comput. Chem. **41**, 1931 (2020).

[47] R. Dronskowski and P. E. Bloechl, Crystal orbital Hamilton populations (COHP): Energy-resolved visualization of chemical bonding in solids based on density-functional calculations, J. Phys. Chem. **97**, 8617 (1993).

[48] S. Jiang, L. Li, Z. Wang, K. F. Mak, and J. Shan, Controlling magnetism in 2D CrI_3 by electrostatic doping, Nat. Nanotechnol. **13**, 549 (2018).

[49] S. Fu, K. Kang, K. Shayan, A. Yoshimura, S. Dadras, X. Wang, L. Zhang, S. Chen, N. Liu, A. Jindal, X. Li, A. N. Pasupathy, A. N. Vamivakas, V. Meunier, S. Strauf, and E. H. Yang, Enabling room temperature ferromagnetism in monolayer MoS_2 via in situ iron-doping, Nat. Commun. **11**, 2034 (2020).

[50] A. S. Dhoot, C. Israel, X. Moya, N. D. Mathur, and R. H. Friend, Large Electric Field Effect in Electrolyte-Gated Manganites, Phys. Rev. Lett. **102**, 136402 (2009).

[51] B. Huang, G. Clark, D. R. Klein, D. MacNeill, E. Navarro-Moratalla, K. L. Seyler, N. Wilson, M. A. McGuire, D. H. Cobden, D. Xiao, W. Yao, P. Jarillo-Herrero, and X. Xu, Electrical control of 2D magnetism in bilayer CrI_3, Nat. Nanotechnol. **13**, 544 (2018).

[52] Y. Feng, N. Liu, and G. Gao, Spin transport properties in Dirac spin gapless semiconductors Cr_2X_3 with high Curie temperature and large magnetic anisotropic energy, Appl. Phys. Lett. **118**, 112407 (2021).

[53] J.-Y. You, X.-J. Dong, B. Gu, and G. Su, Electric field induced topological phase transition and large enhancements of spin-orbit coupling and Curie temperature in two-dimensional

ferromagnetic semiconductors, Phys. Rev. B **103**, 104403 (2021).

[54] N. C. Frey, A. Bandyopadhyay, H. Kumar, B. Anasori, Y. Gogotsi, and V. B. Shenoy, Surface-engineered MXenes: Electric field control of magnetism and enhanced magnetic anisotropy, ACS Nano **13**, 2831 (2019).

[55] L. Webster and J.-A. Yan, Strain-tunable magnetic anisotropy in monolayer $CrCl_3$, $CrBr_3$, and CrI_3, Phys. Rev. B **98**, 144411 (2018).

[56] H. Sheng, H. Long, G. Zou, D. Bai, J. Zhang, and J. Wang, Magnetic and phonon transport properties of two-dimensional room-temperature ferromagnet VSe_2, J. Mater. Sci. **56**, 15844 (2021).

[57] S. Memarzadeh, M. R. Roknabadi, M. Modarresi, A. Mogulkoc, and A. N. Rudenko, Role of charge doping and strain in the stabilization of in-plane ferromagnetism in monolayer VSe_2 at room temperature, 2D Mater. **8**, 035022 (2021).

[58] H. Idzuchi, A. E. Llacsahuanga Allcca, X. C. Pan, K. Tanigaki, and Y. P. Chen, Increased Curie temperature and enhanced perpendicular magneto anisotropy of $Cr_2Ge_2Te_6$/NiO heterostructures, Appl. Phys. Lett. **115**, 232403 (2019).

[59] W. R. Liu, X. J. Dong, Y. Z. Lv, W. X. Ji, Q. Cao, P. J. Wang, F. Li, and C. W. Zhang, Magnetic anisotropy and ferroelectric-driven magnetic phase transition in monolayer $Cr_2Ge_2Te_6$, Nanoscale **14**, 3632 (2022).

[60] S. B. Chen, C. X. Huang, H. S. Sun, J. F. Ding, P. Jena, and E. J. Kan, Boosting the Curie temperature of two-fimensional semiconducting CrI_3 monolayer through van der Waals heterostructures, J. Phys. Chem. C **123**, 17987 (2019).

[61] J. K. Hu, J. X. Tan, D. Wu, Z. H. Zhang, and Z. Q. Fan, Exploring magnetic stability and valley splitting on CrI_3/SiC van der Waals heterostructure, App. Surf. Sci. **560**, 149858 (2021).

[62] J. Bardeen and W. Shockley, Deformation potentials and mobilities in non-polar crystals, Phys. Rev. **80**, 72 (1950).

[63] B. Radisavljevic, A. Radenovic, J. Brivio, V. Giacometti, and A. Kis, Single-layer MoS_2 transistors, Nat. Nanotechnol. **6**, 147 (2011).

[64] Y. Huang, X. Zhong, H. Yuan, and H. Chen, Thermoelectric performance of $MoSi_2As_4$ monolayer, Europhys. Lett. **137**, 16002 (2022).

[65] M. Shi, P. Mo, J. Lu, and J. Liu, Strain-enhanced electron mobility and mobility anisotropy in a two-dimensional vanadium diselenide monolayer, J. Appl. Phys. **126**, 044305 (2019).

[66] Z. Guo, J. Zhou, L. Zhu, and Z. Sun, MXene: A promising photocatalyst for water splitting, J. Mater. Chem. A **4**, 11446 (2016).

[67] Y. Kim, S. Kim, H. Cho, Y. M. Kim, H. Ohta, and K. Char, Transport Properties of the $LaInO_3/BaSnO_3$ Interface Analyzed by Poisson-Schrödinger Equation, Phys. Rev. Appl. **17**, 014031 (2022).

[68] L. Pfeiffer, K. W. West, H. L. Stormer, and K. W. Baldwin, Electron mobilities exceeding 10^7 cm^2/Vs in modulation-doped GaAs, Appl. Phys. Lett. **55**, 1888 (1989).

[69] O. Ambacher, J. Smart, J. R. Shealy, N. G. Weimann, K. Chu, M. Murphy, W. J. Schaff, L. F. Eastman, R. Dimitrov, L. Wittmer, M. Stutzmann, W. Rieger, and J. Hilsenbeck, Two-dimensional electron gases induced by spontaneous and piezoelectric polarization charges in N- and Ga-face AlGaN/GaN heterostructures, J. Appl. Phys. **85**, 3222 (1999).

[70] Z. Cai, M. Li, and L. Fan, Sheet carrier density dependent Rashba spin splitting in the $Al_{0.5}Ga_{0.5}N/GaN/Al_{0.5}Ga_{0.5}N$ quantum well, J. Semicond. **35**, 092002 (2014).

[71] S. Thiel, G. Hammerl, A. Schmehl, C. W. Schneider, and J. Mannhart, Tunable quasi-two-dimensional electron gases in oxide heterostructures, Science **313**, 1942 (2006).

[72] U. Kim, C. Park, Y. M. Kim, J. Shin, and K. Char, Conducting interface states at $LaInO_3/BaSnO_3$ polar interface controlled by Fermi level, APL Mater. **4**, 071102 (2016).

[73] G. Brammertz, H. C. Lin, M. Caymax, M. Meuris, M. Heyns, and M. Passlack, On the interface state density at $In_{0.53}Ga_{0.47}As$/oxide interfaces, Appl. Phys. Lett. **95**, 202109 (2009).

[74] V. I. Zubkov, Simulation of capacitance-voltage characteristics of heterostructures with quantum wells using a self-consistent solution of the Schrödinger and Poisson equations, Semiconductors **40**, 1204 (2006).

[75] B. Hu, Modeling accumulation capacitance-voltage characteristic of MoS_2 thin flake transistors, Semicond. Sci. Technol. **30**, 055013 (2015).

[76] H. Kroemer, W. Y. Chien, J. S. Harris, and D. D. Edwall, Measurement of isotype heterojunction barriers by CV profiling, Appl. Phys. Lett. **36**, 295 (1980).